RSC Advances

ARTICLE

One-step electrodeposition of a self-cleaning and corrosion resistant Ni/WS_2 superhydrophobic surface

Received 00th January 20xx,
Accepted 00th January 20xx

DOI: 10.1039/x0xx00000x

www.rsc.org/

Guochen Zhao,[a,b] Yanpeng Xue,[c] Yuanfeng Huang,[d] Ying Ye,[d] Frank C Walsh,[b] Jie Chen*[a] and Shuncai Wang*[b]

Superhydrophobic surfaces have been intensively investigated for applications requiring self-cleaning and corrosion resistance. The techniques used to fabricate such a coating tend to be costly, time and energy consuming; further surface modification steps are often needed. In this study, a superhydrophobic composite electrodeposit based on a tungsten disulphide nanoparticles dispersed in nickel on a mild steel substrate was successfully developed. At room temperature, the deposit showed a water contact angle of 158.3 deg and sliding angle of 7.7 deg. The effects of operational parameters on surface morphology and superhydrophobicity are discussed. Compared to the substrate, the robust surface of the as-prepared coatings exhibited good self-cleaning and corrosion resistance, providing potential for industrial applications.

Introduction

Due to their potentially high impact on industry, superhydrophobic surfaces, having a minimum 150 deg contact angle and maximum 10 deg sliding angle for water droplets, have attracted intense attention over the last decade. Research and develop-ment subject areas related to superhydrophobicity include anti-corrosion,[1, 2] antifouling,[3] anti-icing,[4] self-cleaning,[1, 5] oil-water separation,[6] friction reduction,[7] and energy saving.[7, 8]

Many methods have been successfully applied to fabricate superhydrophobic surfaces, including etching, lithography, airless and solvent spraying, chemical vapour deposition, sol-gel synthesis, surface oxidation and a variety of templating. Currently, most of these coatings are prepared from low surface energy organic materials.[2, 9, 10] However, these organic materials have limitations in engineering applications due to their inherent instability. Inorganic materials are therefore important for robust superhydrophobic coatings. Ceramics are particularly important due to their good mechanical strength and heat/corrosion resistances. Although ceramics are rarely used for water-repelling surfaces because of their intrinsically hydrophilic nature, our group has recently prepared a ceramic TiO_2/BN coating with superhydrophobic contact angle of nearly 170 deg by thermal spraying[11]. Its superhydrophobicity has been maintained over a year but the process is relatively costly. In contrast, electrodeposition, having the benefits of facile operation, moderate costs and reproducibility, is a more appropriate technique to produce water-repellent surfaces for engineering applications. The reported cases included Ce/Mn myristates mineral,[2, 9] however, up to now the superhydrophobic coatings created by this technique tend to be deposited using high currents (and high cell voltages), which can result in loosely adherent, non-compact coatings.[1, 2, 12, 13]

Nickel (Ni) deposits, as one of the dominant family of replacement coatings for hard chromium, have been extended to diverse applications, ranging from tribological functions such as corrosion-resistance, super-hardness and wear resistance to thin films for bulk electroformed products.[14] Several groups have reported the superhydrophobicity of Ni-based electrodeposits.[1, 15-20] Esmailzadeh et al. deposited the superhydrophobic nickel coating via two-step electrodeposition.[18] Tian et al. fabricated a superhydrophobic nickel surface by coupling electro and electroless deposition.[19] Liang et al. and Chen et al. modified the superhydrophobic nickel-based coating using organic FAS-13[15] and myristic acid[20] respectively. In summary, these coatings were prepared either by relatively complex electrodeposition (i.e. two-steps), electroless deposition but challenges on keeping stable chemical solutions or by use of organics. In this study, we aim to obtain the robust metal ceramic composite coatings (Ni-WS_2) via a one-step process, extending applications in superhydrophobicity through cost effective and repeatable electrodeposition.

Hierarchical morphologies, presenting microroughness covered with nanoroughness, have been suggested as essential elements in achieving a high contact angle.[21] Addition of hexadecyltrimethylammonium bromide (CTAB) as surfactant and saccharin as grain refiner to the bath enables an optimised microrough structure to be obtained. Inclusion of nanoparticles is also important to control the nanoroughness. Ceramics with

[a] School of Environmental and Chemical Engineering, Shanghai University, Shanghai, 200444, China. Email: jchen@shu.edu.cn, Tel: +86(0)2166137482
[b] National Centre for Advanced Tribology at Southampton (nCATS), University of Southampton, SO17 1BJ, UK. Email: wangs@soton.ac.uk, Tel: +44 (0)2380594638
[c] Chemistry, Natural and Environmental Sciences, University of Southampton, SO17 1BJ, UK
[d] Ocean College, Zhejiang University, 316021, China

low surface energies are further considered, for which the layer structured materials including MoS_2, WS_2, $MoSe_2$, BN fall in the range 65-75 mJ m^{-2} and graphene at 65-120 mJ m^{-2}.[22] Tungsten disulphide nanoparticles (WS_2 NPs) have been used to fabricate super-hydrophobic coatings in this study as they exhibit high thermal stability, good oxidation resistance, low friction coefficient and low surface energy. García-Lecina et al. have successfully prepared the Ni-WS_2 coatings by electrodeposition but with high coefficient friction (0.50) which indicates that an insufficient quantity of WS_2 was incorporated. [23] In this study we aim to fabricate a robust superhydrophobic coating and thus used some different parameters including current density, solution agitation, pH of bath, concentration of additives. We used a deposition temperature of 40 degC which was much lower than 55 degC used by García-Lecina et al. work. This will save energy and importantly reduce chemical evaporation and thus improve the working environment. Furthermore, corrosion performance is an always important part of coatings and thus the effect of WS_2 has been investigated in the study.

Electrodeposition was carried out in a Watts nickel bath having a controlled WS_2 content. The process was one-step thus time-saving, without the need to modify the coating by application of low surface energy organics. The robust coating surface presents a "lotus effect"[24] which has been deployed in anti-corrosion and self-cleaning applications.

Experimental procedure

Sample preparation

Nickel sulphate ($NiSO_4 \cdot 6H_2O$, Sigma–Aldrich), nickel chloride ($NiCl_2 \cdot 6H_2O$, Sigma–Aldrich) and boric acid (H_3BO_3, HOC(COOH)-$(CH_2COOH)_2$, Sigma–Aldrich) were dissolved into 1 dm^3 purified water as the basic solution. The pH value of the solution was maintained at 3.5±0.2 by adding HCl or NaOH. The base electrolyte is similar to a typical nickel Watts bath. Different amounts of tungsten disulphide nanoparticles (WS_2 NPs, 200 nm, Shanghai ST-NANO Science & Technology Co., Ltd) were dispersed in the aqueous bath, in addition to hexadecyltrimethylammonium bromide (CTAB, $CH_3(CH_2)15N(Br)(CH_3)_3$, Sigma–Aldrich) and saccharin (Sigma–Aldrich). CTAB is a kind of cationic surfactant which has a hydrophobic tail and a positive-charged hydrophilic head. In the process of electrodeposition, CTAB is used to not only disperse WS_2 nanoparticles but also charge the particles, which helps with the deposition of the cationic particles onto the cathode substrate. Before electrodeposition, the WS_2 particles were dispersed in an ultrasonic water bath for 10 min to reduce agglomeration. The composition of the electrodeposition bath is shown in Table 1.

Table 1. Composition of the electrodeposition bath

Component	Concentration / g dm^{-3}
$NiSO_4 \cdot 6H_2O$	250
$NiCl_2 \cdot 6H_2O$	45
H_3BO_3	40
CTAB	0.1
WS_2	1, 5, 10, 15, 20
Saccharin	1.5

Nickel and mild steel plates were used for the anode and cathode electrode, respectively. The 3 mm thick mild steel substrate was wet polished down to 800 SiC paper then activated by immersion in a 10% vol. HCl solution at 20 ℃ for 10 seconds followed by rinsing in pure water at 20 ℃. The electrodeposition was carried out at a constant temperature of 40 ℃ under stirring by a cylindrical, PTFE-coated steel magnetic follower of 6 mm diameter and 25 mm length rotating at 100 rpm located centrally at the bottom of a 200 mL cylindrical beaker. The current density was 4 A dm^{-2} and the vertical, parallel electrodes were 25 mm apart. The effects of different concentrations of WS_2 NPs and controlled deposition times were investigated.

Deposit characterisation

All water contact angle and sliding angle measurements used 5 microlitre purified water droplets using a measuring apparatus (DSA100, Germany) at 20 ℃. The contact angle was measured by DropSnake which is a plugin of ImageJ (software) to shape the drop.[25, 26] Each value was the average measurement of 5 different positions on the same sample surface. Surface morphologies of various samples were studied by field emission scanning electron microscope (JEOL JSM 6500F, Japan). The chemical compositions of the samples were investigated with X-ray diffraction (Bruker D2 PHASER diffractometer, Germany) and energy dispersive X-ray spectroscopy (Oxford X-Max SDD, UK).

A corrosion monitoring instrument (Gill AC ACM, UK) was used to observe the electrochemical corrosion of the coating. A platinum plate was used as the counter electrode with a saturated calomel electrode (SCE) as the reference electrode. The coated mild steel was used as the working electrode and the exposed area was controlled at 1 ±0.1 cm^2. The measurements were performed in 3.5% wt. NaCl solution at 25 ℃ The anodic polarization curves were recorded at a linear potential scan rate of 0.5 $mV \cdot s^{-1}$ from −250 to 250 mV vs. SCE from the open-circuit electrode potential.

Self-cleaning studies utilised a dust of yellow $CaCO_3$ chalk particles and purified water. The video (240 fps) and still images were captured by a digital camera (8-megapixel iSight camera with 1.5µ pixels).

Results and discussion

Wettability and surface morphology

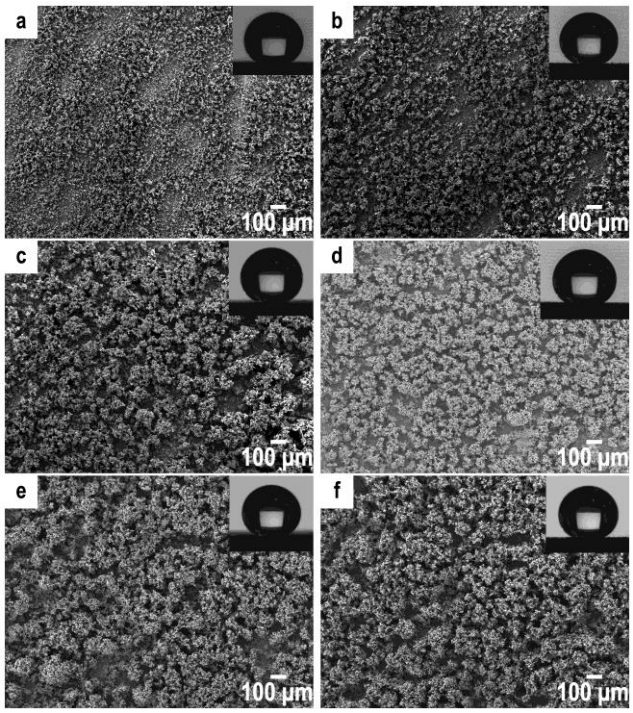

Fig. 1 The surface morphologies influenced by different current densities (free of saccharin). (a) 2 A dm^{-2}; (b) 3 A dm^{-2}; (c) 4 A dm^{-2}; (d) 5 A dm^{-2}; (e) 6 A dm^{-2}; (f) 7 A dm^{-2}.

Table 2. The contact angles of coatings with applied different current densities. (1, free of saccharin; 2, addition of saccharin. Deposition time: 30 min)

Current density / A dm^{-2}	3	4	5	6	7
Contact angle 1 / deg	156.5	158.1	150.3	153.4	150.8
Contact angle 2 / deg	143.6	157.7	154.8	155.7	153.9

Current density is one of the key parameters for electrodeposition and 4 A dm^{-2} is commonly used for the Ni-based coatings electrodeposition [e.g. ref[27]]. A lower current density leads a low deposition rate, and a higher current density results in a loose coating structure. In this study, we prepared coatings using current densities of 2, 3, 4, 5, 6, 7 A dm^{-2} (without saccharin addition), with SEM images of the surfaces displayed in Fig. 1. They show the growth of protruding clusters with increasing current density. The average diameters of clusters were estimated by ImageJ to be 35.6 µm (2 A dm^{-2}), 48.8 µm (3 A dm^{-2}), 73.9 µm (4 A dm^{-2}), 96.7 µm (5 A dm^{-2}), 103.2 µm (6 A dm^{-2}), 112.9 µm (7 A dm^{-2}). The inset in each image show the superhydrophobic water drop with contact angles listed in Table 2. This demonstrates that the superhydrophobic coatings can be readily prepared using a range of current densities, although the highest contact angle was achieved at the current density of 4 A dm^{-2}.

Table 3. Influence of electrodeposition from a bath containing dispersed WS_2 NPs on WS_2 content in coatings

Concentration of WS_2 in bath / g dm^{-3}	1	5	10	15	20
WS_2 content in coatings / wt. %	0.96	2.46	4.88	10.91	9.39

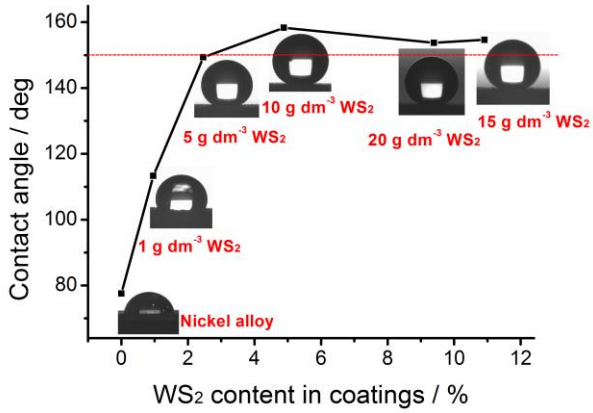

Fig. 3 Water contact angle on the surface of coatings with different WS_2 content. Red footnote indicate the concentration of WS_2 in bath.

With saccharin added into the electrodeposited solutions, the coatings had more dense structures, which could be observed by comparison between Fig. 1(c) and Fig. 2(d) using the same current density of 4 A dm^{-2} for example. However, the saccharin did not appear to have much influence on the contact angles. The majority of the coatings in Table 2 show their superhydrophobicity. Considering the dense structure and slightly higher contact angle being achieved, the current density 4 A dm^{-2} was fixed after.

Controlled concentrations of WS_2 were included into Ni electrodeposits to optimise their hydrophobicity. Fig. 2 shows the surfaces of the coatings prepared after 30 min electrodeposition in the bath with the concentrations of 0, 1, 5, 10, 15 and

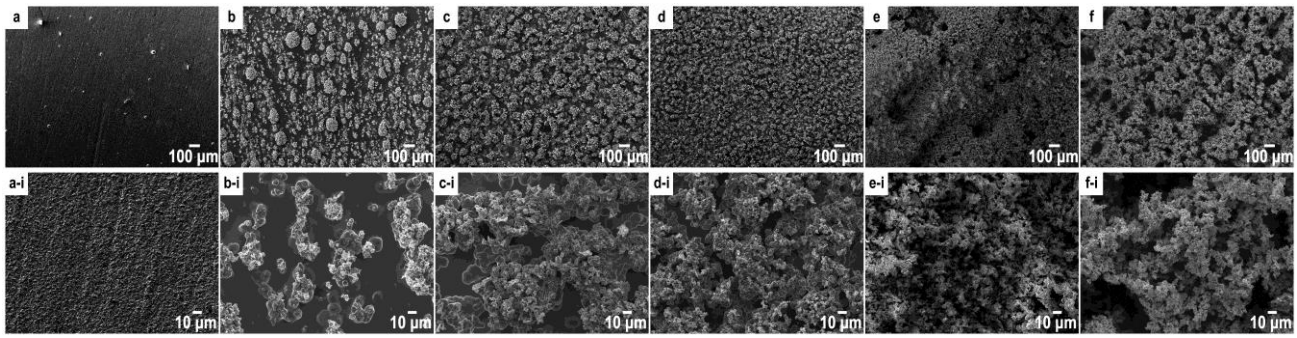

Fig. 2 SEM images of coatings from baths containing controlled WS_2 concentrations. (a) zero; (b) 1 g dm^{-3}; (c) 5 g dm^{-3}; (d) 10 g dm^{-3}; (e) 15 g dm^{-3}; (f) 20 g dm^{-3}. (a-i), (b-i), (c-i), (d-i), (e-i), (f-i) are the corresponding high magnification images.

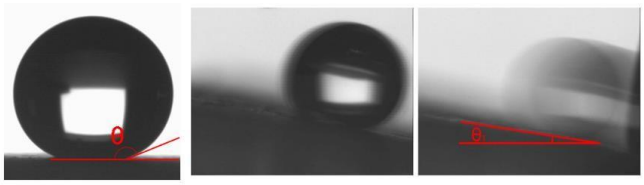

Fig. 4 Static contact angle (θ) of pure water droplets and sliding angle (θ_T) on the superhydrophobic coating deposited for 30 min from a bath containing 10 g dm^{-3} WS_2.

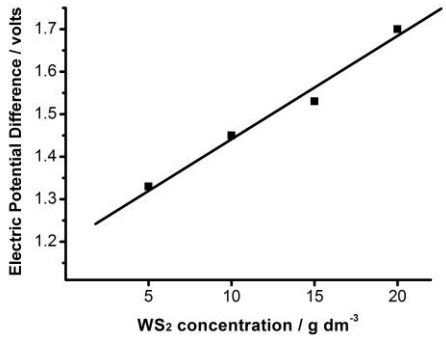

Fig. 5 The increasing cell voltage resulted from a higher WS_2 concentration dispersed in the bath.

Table 4. Conductivities of the electrodeposition bath

Concentration of WS_2 / g dm^{-3}	Electrolytic conductivity / S m^{-1}
1	9.02
5	8.27
15	7.85
20	7.06

20 g dm^{-3} WS_2. The pure Ni coating formed smooth surface (Fig. 2 (a)). With the WS_2 concentration increased, the surface roughness were transformed from coarse in Fig. 2(b) and 2(c), fine in Fig. 2(d) and 2(e) then to porous surfaces in Fig. 2(f). This is more evident at higher magnification. In the absence of WS_2 NPs, the coating showed fine Ni crystals in Fig. 2(a-i). At the bath concentration of 1 g dm^{-3} WS_2, the composite coating surface showed a protruding surface with WS_2 clusters attached in Fig. 2(b-i). A similar morphology with more nodules and clusters can be observed in Fig. 2(c-i) at a 5 g dm^{-3} WS_2 bath concentration. This situation was improved while applying WS_2 concentration of 10, 15 and 20 g dm^{-3} in Fig. 2(d-i), (e-i), (f-i). Many holes appeared on the surface of the electrodeposit from a bath containing 15 g dm^{-3} WS_2 in Fig. 2(e-i) coating and, particularly for the coating from a 20 g dm^{-3} WS_2 bath in Fig. 2(f-i).

The wettability of coatings is affected by two parameters i.e. surface roughness and surface energy.[28] Pure Ni alloy with high surface energy has a contact angle of 77.6 deg. WS_2 in coating is the main substance to reduce the surface energy of coating. Table 3 shows differing concentrations of WS_2 in bath with the resultant WS_2 content achieved in the coatings after deposition. It can be seen that the content of WS_2 increases with higher concentration of WS_2 until the maximum of 10.9 wt. % at 15 g dm^{-3}. It then decreased to 9.4 wt. % at 20 g dm^{-3}. This could be explained by the absorption effect.[29] Meanwhile, Fig. 3 illustra-tes the contact angles against various WS_2 contents in the coatings. The non-uniform structures with lower WS_2 content in Fig. 2(b) and (c) showed hydrophobicity with contact angles of 92.9 deg and 148.8 deg. The water-repellent property was enhanced as the content of WS_2 increased on the surface. Superhydrophobicity was shown in the coatings above 4 wt. % WS_2, with water contact angles between 153.8-158.3 deg. The coating with 4.88 wt. % WS_2 deposited on the surface showed the highest contact angle of 158.3 deg and a sliding angle of 7.7 deg, as shown in Fig. 4. In this study, the water drops on the majority of the coatings were actually sliding less than 5 deg, however. According to the report from Watanabe et al., sliding angle could be influenced by roughness, surface energy and the mass of droplet.[30] The high water contact angle and the low sliding angle indicate that the water droplet can easily roll down the surface when it tilts,[31] which is attributable to the "lotus effect". The precise coordination of the roughness and the interfacial chemistry response are the two parameters contributes to the droplet mobility switching.[32] The hydrophobicity improved in comparison with the original mild steel substrate 91.9 deg (Video 1). Combined with Fig. 2, it can be inferred that the water contact angle is dependent on the surface morphology as well as WS_2 content of the coating.

Fig. 5 shows that the potential difference between the anode and cathode, i.e., the cell voltage, increased with the WS_2 concentrations in the bath. The more WS_2 in the bath caused a decrease on bath conductivity. The conductivities of various baths can be found in Table 4. A high cell voltage indicated a high negative overpotential at the cathode and resulted in intensive hydrogen evolution which blocked the deposition of particles and metal.[27] Subsequently, the hydrogen bubbles promoted the generation of abnormal holes in Fig. 2(d) (15 g dm^{-3} WS_2 NPs) and Fig. 2(f) (20 g dm^{-3} WS_2 NPs), which contributed to a slight decrease in the contact angles in Fig. 3. The size, height and the distance of hierarchical micro-nano structure affect the wettability of the hydrophobic surface.[33] The coating (i.e. Fig. 2(d)) with appropriate structure can

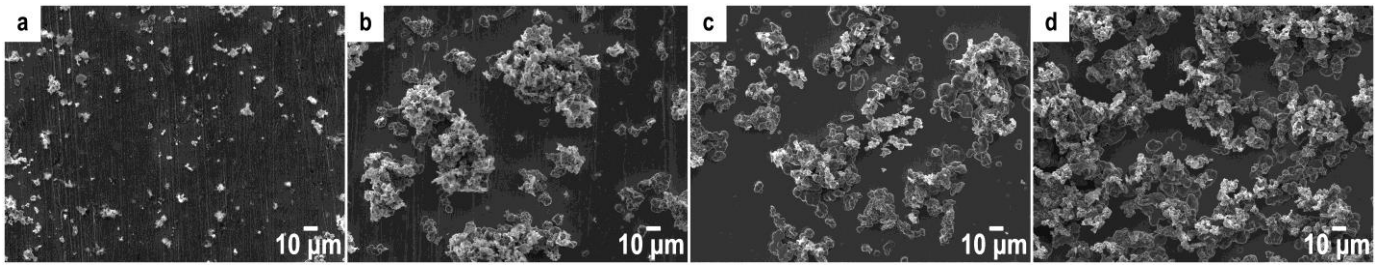

Fig. 6 SEM images of coatings from a bath containing 10 g dm^{-3} WS_2 after (a) 1 min, (b) 5 min, (c) 10 min and (d) 20 min.

prevent the penetration of water droplets and thus minimise the contact area of the droplet and the coating. This resulted in the formation of an air layer on the interface, which is consistent with the Cassie model. For the coatings 2(d) and 2(f), due to the presence of holes which is equivalent to increasing microroughness, the droplet tends to penetrate and invade the holes. Thus, the proportion of area of solid-liquid interface increased. According to the Cassie statement, the apparent contact angle should be reduced.

The surface morphologies of coatings at electrodeposition times of 1 min, 5 min, 10 min and 20 min are shown in Fig. 6. After the first minute, the substrate was sparsely covered by WS_2 NPs dispersed in the thin Ni matrix in Fig. 6(a). After 5 min, the non-uniform aggregate structures ranging from 2 µm to 100 µm were formed in Fig. 6(b). The existences of lines were traces of scratches formed by SiC paper grinding. The WS_2 NPs attached on the electrode will maintain electrical conductivity with the Ni matrix and the high concentration of WS_2 induced a higher deposition rate. After 10 min, the line scratches were fully covered by the fresh deposit. The superhydrophobicity appeared after deposition times longer than 20 min, as shown in Fig. 7b, the corresponding coatings showed robust surfaces.

Cross-sectional observations would help to clarify the deposition mechanism as well as to estimate the coating thickness. However, soft WS_2 would be elongated by grinding and polishing. To preserve its original structure, the sample was broken down after being held in liquid nitrogen for 5 minutes. The fractured surface was subsequently observed in SEM. As shown in Fig. 7a, the coarse areas are WS_2 rich (confirmed by EDS) deposited throughout the whole cross-section. It also shows that equal-axis grains were developed during the deposition. The coating thickness after 30 min electrodeposition was ~45 microns.

Fig. 8 shows the lotus-like structure on the superhydrophobic surface while Fig. 10 illustrates the details of contact area between a stable water droplet and the surface of coating. After 30 min electrodeposition, the microstructure in Fig. 8(a) of 6.6 µm and nanostructured 150 nm particles were formed in Fig.8(b).

In order to identify the distribution of Ni and WS_2 NPs on the lotus-like structure, an EDS mapping was carried out. As showed in Fig. 9, in the hierarchical composite structure, nickel covered the whole surface of the coating. Element sulphur was mainly located in the micro-nano structured area (lotus-like). Due to the low resolution of x-ray detector (about 150 eV), nickel could interfere the location of W. The accurate location of WS_2 NPs should be coincident with S, which is mainly on the clusters.

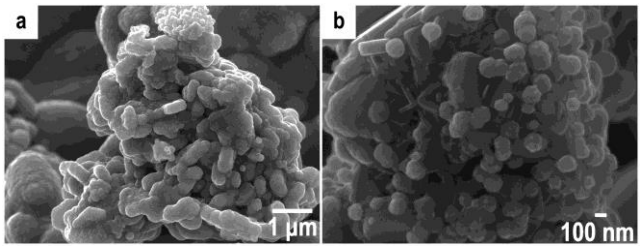

Fig. 8 lotus-like high magnification deposit images captured from the sample which was deposited with 10 g dm^{-3} WS_2 NPs.

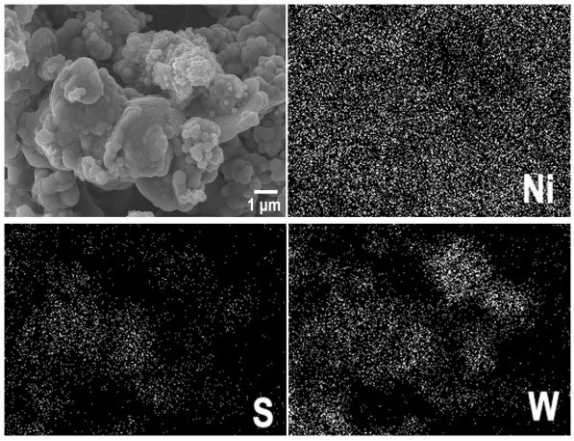

Fig. 9 EDS mapping of the micro-nano structure.

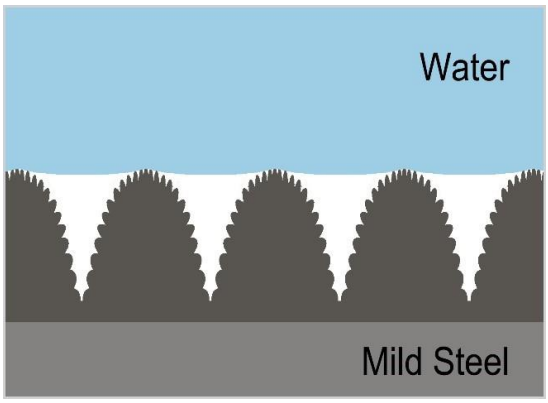

Fig. 10 A schematic illustration of contact area, in which air is entrapped underneath a water droplet on the surface.

Table 5. Percentages of solid-liquid interface (f_{SL}) and liquid-air interface (f_{LA}) in a plane geometrical contact area calculated from the Cassie–Baxter equation.

Sample	Contact Angle / deg	$\%f_{SL}$	$\%f_{LA}$
30 min from 15 g dm^{-3} WS_2	154.7	7.83	92.17
30 min from 20 g dm^{-3} WS_2	153.8	8.39	91.61
20 min from 10 g dm^{-3} WS_2	156.9	6.55	93.45

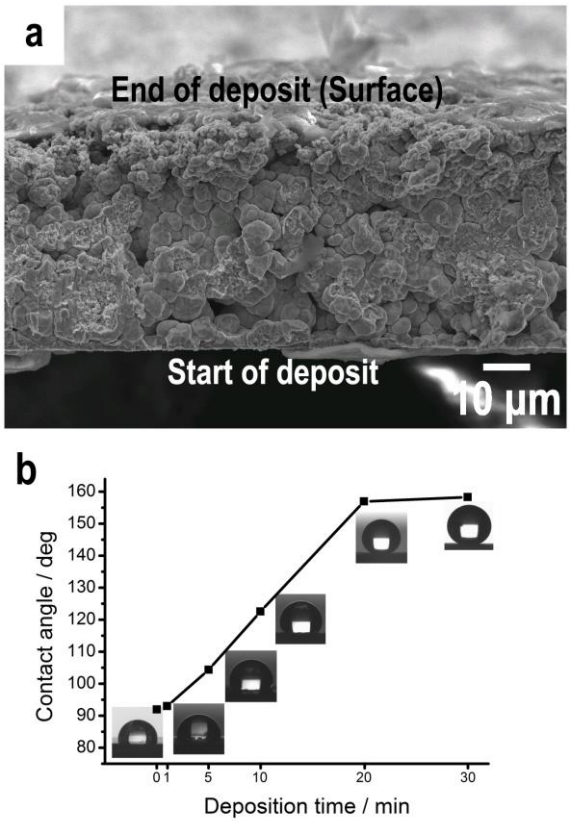

Fig. 7 a) Cross-sectional image of coating after 30 min electrodeposition. b) Influence of electrodeposition time on the contact angle for water on the superhydrophobic surface.

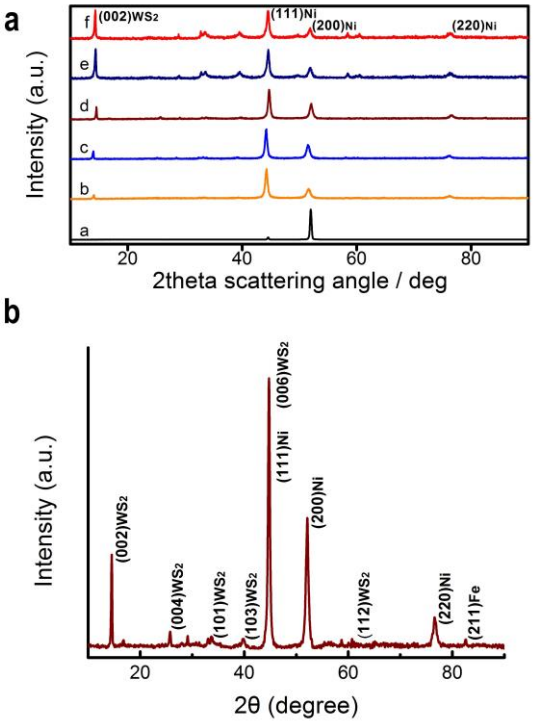

Fig. 11 a) X-ray diffraction patterns of the different investigated coatings. (a)Pure Ni coating; (b) coating from bath containing 1 g dm^{-3} WS_2; (c) coating from bath containing 5 g dm^{-3} WS_2; (d) coating from bath containing 10 g dm^{-3} WS_2; (e) coating from bath containing 15 g dm^{-3} WS_2; (f) coating from bath containing 20 g dm^{-3} WS_2. b) X-ray diffraction patterns of deposit after 30 min from a bath containing 10 g dm^{-3} WS_2 NPs.

According to the Wenzel-Cassie model [34], when the water droplet touched the lotus-like surface, an air layer remains in the micro gaps preventing water ingress [2]. The water droplet is suspended on the surface due to contacting both the solid substrate and gas phase (white area). Based on the Cassie–Baxter equation, the apparent contact angle θ should be described by:

$$\cos\theta = f_{SL}\cos\theta_y + f_{LA}\cos\theta_A \quad (1)$$

where f_{SL} and f_{LA} are the total area of solid-liquid interface and the total area of liquid-air interface in a plane geometrical area of unity parallel to the rough surface. θ_y, θ_A is the Young's contact angle for an ideal solid surface and the contact angle with the gas phase, respectively. The contact angle of water droplet with air is 180 deg. Ideally, if the droplet is small enough to neglect the effect of gravity and the dendrites are dense to make the water-air contact line parallel to the rough surface, then $f_{SL} + f_{LA} = 1$. From the θ_y value at approximately 77 deg measured on the pure smooth Ni coating, it can be calculated that the as-prepared superhydrophobic coating has contact angle of 158.3 deg about 5.8% area of the water contacted the coating while 94.2% was in contact with air. The percentages for other as-prepared lotus state coatings are listed in Table 5.

Coating textures

Fig. 11(a) shows the XRD patterns of Ni (JCPDS 04-0850) and Ni-WS_2 composite coatings containing various concentrations of WS_2 NPs (JCPDS 08-0237), which have been Miller indexed. According to the standard data from JCPDS, two diffraction peaks of nickel at 2Theta equal to 44.51 deg and 51.85 deg are attributed to the (111) and (200) Bragg reflections of the face-centred cubic (fcc) structure of metallic nickel. For WS_2, the peaks at 14.32 deg, 39.55 deg and 33.57 deg are attributed to the (111), (103) and (101) of hexagonal closed-packed (hcp) structure. As Fig. 11(a) demonstrated, the preferred orientation of Ni crystal was changed. The pure Ni coating in Spectrum a) shows a strong texture with (200) plane parallel to the coating surface. It can be elucidated by minimising the interface energy between the mild steel substrate and the Ni coating during nucleation and growth of Ni crystals. The Ni composite coatings however tend to grow (111) planes parallel to the coating surface.

Saccharin changed the preferred orientation of nickel crystal from (200) to (111).[14, 35-37] It also acted as the grain refiner to make the clusters smaller which may enhance the anti-abrasion property and long-term stability. Furthermore WS_2 NPs affected the preferred orientation.[23] Similar observations were reported in other composite films with the incorporation of the ceramic particles, such as WC [38], SiC, Al_2O_3 [39] etc. The growth of $(111)_{Ni}$ plane parallel to the surface is driven by minimisation of surface energy. A peak diffracted from the (002) plane of WS_2 enhanced steadily at progressively higher WS_2 particle concentrations in the bath in Spectrums (c-g). This indicated that a high concentration of WS_2 in the bath contributes to the electrodeposition of NPs.

One XRD pattern for the coating from a bath containing 10 g dm^{-3} WS_2 was enlarged, as shown in Fig. 11(b). The peak at 44 deg can be indexed by $(111)_{Ni}$ and $(006)_{WS2}$. The spacing

difference between two planes is calculated to be less than 1%. This means the (111) of nickel crystals readily grow on (002) plane of WS_2 NPs which have already attached on the substrate.

Abrasion test

The coatings appear porous on the micron scale, but they are certainly not in macroscale. One optical picture in Fig. 12a confirms its dense/compact coating (10 g dm^{-3} WS_2, 30min). Such a robust coating has been left at room temperature for 10 months but still remains it superhydrobicity.

A further test investigated the mechanical stability by abrasion. As shown in Fig. 12b, a weight of 100g was loaded in a 400 grit SiC sandpaper which was placed face down and repeatedly moved on the coating surface. Assuming a flat surface, the pressure applied on the coating can be calculated as 2.83×10^3 Pa. The real surface, however, is much rough and therefore the pressure must be much higher.

Each contact angle after a fixed abrasion length was measured as shown in Fig. 12c. It was confirmed that the Ni-WS_2 coating kept its superhydrophobicity over 150 deg within the duration of 1250 mm. After this stable stage, the coating gradually loses it superhydrophobicity with the contact angle just under 140 deg after 2500 mm. This abrasive data showed a better result than most of coatings. For instance, the nickel-based superhydrophobic coatings on magnesium alloy modified by stearic acid maintained its hydrophobicity in a length of 700 mm under 1.2 kPa abrasive stress. [40]

Corrosion Resistance

The corrosion behaviour of the bare mild steel and the as-prepared electrodeposited coating was investigated by potentiodynamic polarization tests in 3.5 wt. % NaCl aqueous solution at a scanning rate of 0.5 mV s^{-1} (Fig. 13(a)). The corrosion potential (E_{corr}) and the corrosion current density (j_{corr}) are given in Fig. 13(b) using the Tafel extrapolation method applied to the potentiodynamic polarization curves. Fig. 13(b) shows that the corrosion potential and corrosion current density of the bare mild steel are about -0.454 V and 1.21×10^{-5} A cm^{-2}, respectively. For the superhydrophobic Ni coatings with the addition of WS_2 NPs, the corrosion potential shifted positively and the corrosion current densities decreased continuously. When the concentration of WS_2 NPs reached 15 g dm^{-3}, the corrosion potential shifted to -0.162 V *vs.* SCE and the corrosion current density was about 2.07×10^{-7} A cm^{-2}, approximately 58 times less than that of the bare mild steel. The current density of the as-prepared superhydrophobic surface is much lower and the potential is much more positive than that of the electrodeposited Ni coating and achieves the same order of magnitude as that of the Ni but organic modified superhydrophobic surface reported by Su et al.[1] A more positive E_{corr} indicates a lower corrosion tendency and a lower I_{corr} value represents a lower corrosion dynamic rate.[41]

The mechanism of corrosion resistance could probably be related to hydrophobicity of coatings.[1, 2, 41] It can be seen in Fig. 13(b) that as the WS_2 content increased, the current density tended to decrease and the potential became more positive. The hydrophobicity curve (Fig. 3) changed similarly against the

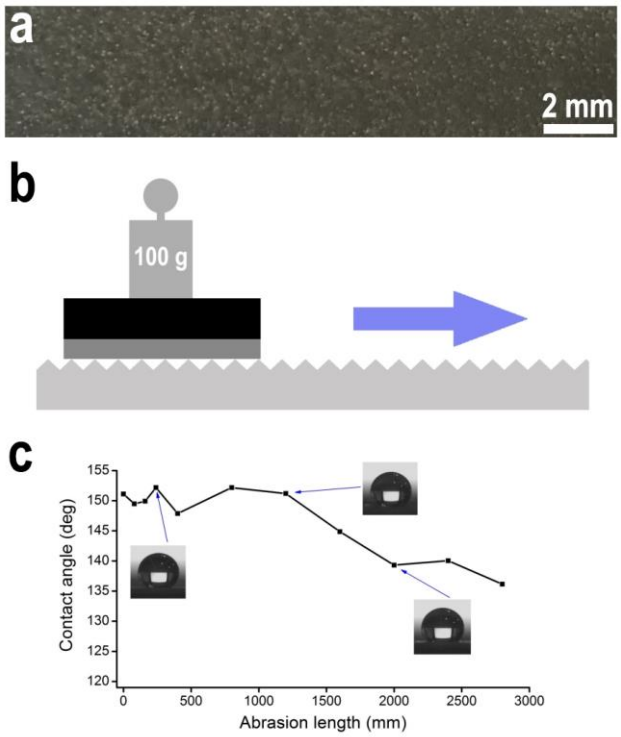

Fig. 12 a) Digital photo of as-prepared superhydrophobic coating. b) The sandpaper abrasion test. c) Influence of abrasion length on contact angle.

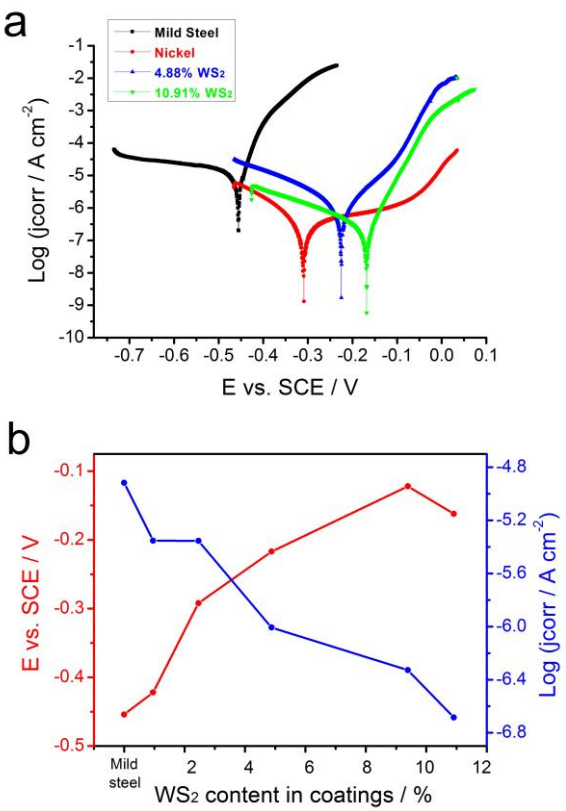

Fig. 13 a) Potentiodynamic polarization curves of the bare mild steel and different electrodeposited coatings from bath containing 0, 10 g dm^{-3}, 15 g dm^{-3} in 25 ℃. b) Corrosion potential (E_{corr}) and corrosion current density (j_{corr}) extracted from polarization curves against WS_2 content.

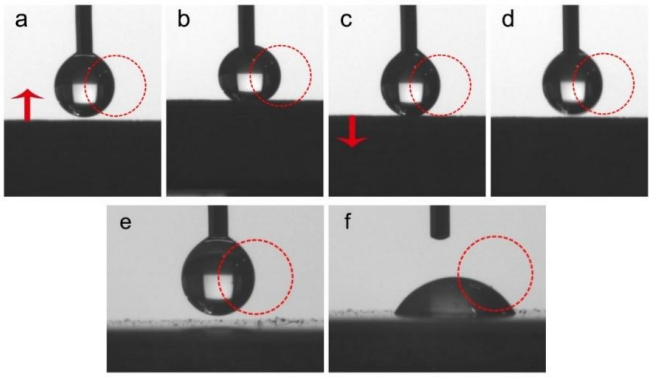

Fig. 14 The qualitative surface energy test on the superhydrophobic surface (a-d) and Ni surface (e-f). The dash red circles as reference represent ideal droplets without outside interference.

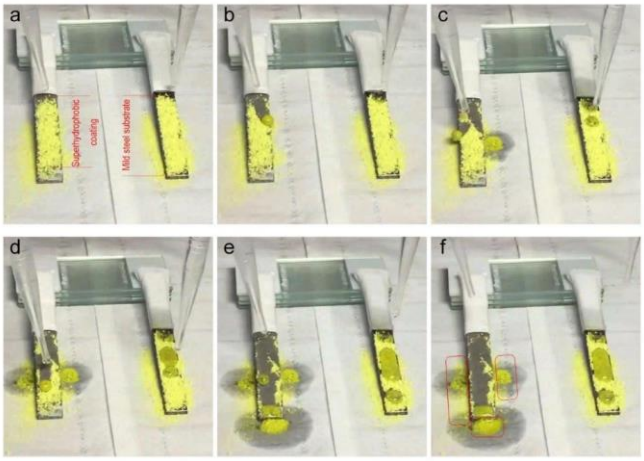

Fig. 15 The process of self-cleaning of an as-prepared superhydrophobic coating (left) in contrast to a bare mild steel substrate (right).

WS_2 contents in the coatings. Due to the low wetted area on solid surface immersed in the aggressive solution, the trapped air between the clusters in the superhydrophobic surface can serve as an effective barrier to keep corrosive media away from the surface and provide better corrosion protection for the bare mild steel. [42] The nanosized particles acting as barriers could give the composite coatings better corrosion resistance than a pure nickel layer.[43]

These results suggest that the superhydrophobic surface of electrodeposited Ni coating with the addition of WS_2 NPs shows better corrosion resistance than the bare mild steel.

Low Adhesion and Self-cleaning

The processes of qualitative surface energy test on the superhydrophobic coating (Fig. 14(a-d)) includes the forwarding and backing ward the coating to a 5 microlitre water droplet. Compared with the red circle, the droplet touched the surface and suffered from a compressive stress. When the coating unattached from the droplet, the droplet suspending on the PTFE syringe needle was difficult to be pulled down to the superhydrophobic surface, which confirmed the low surface energy of the coating (Video 2). In contrast, the droplet tended to adhere on the Ni coating than suspend on the needle in Fig. 14(f).

Self-cleaning is a significant application for superhydrophobic surface.[1, 5, 12] The self-cleaning function of the as-prepared superhydrophobic coating was examined using the yellow chalk debris as contamination markers (Video 3). In contrast, the mild steel substrate was placed on the right in Fig. 15. Both sheets were tilted at a slope of 10 deg above the horizontal and were covered randomly by the dust. The water droplet absorbed the dust immediately which collected on the surface. Due to the low adhesion of the superhydrobic surfaces which have been demonstrated in Fig. 15, the droplet remained spherical in shape, with the attached chalk debris and rolled off the surface in Fig. 15(b), (c) and (d). Subsequently, the surface recovered its superhydrophobicity in Fig. 15(e). A comparison with the mild steel substrate showed that debris adhered on the surface. Contaminants could be easily removed on the as-prepared superhydrophobic coatings.

Conclusions

The self-cleaning and corrosion resistant robust superhydrophobic coating with a water contact angle of 158.3 deg and a sliding angle of 7.7 deg has been successfully fabricated by a facile, single-step electrodeposition. The scanning electron microscope images showed that the superhydrophobicity resulted from its combination of nickel at the roughness of tens of microns and minimum 5 wt.% WS_2 at the scale of 100 nanometers. For the prepared superhydrophobic coatings, the minimum concentration of WS_2 in the bath was 10 g dm^{-3} and the deposition time should exceed 20 min. Potentiodynamic polarization (Tafel curves) in 3.5% wt. aqueous NaCl solution revealed the superhydrophobic coatings have better corrosion resistance. The superhydrophobic coating exhibited excellent self-cleaning properties, which may provide an effective approach in the potential industrial applications of superhydrophobicity using this low-cost, simple and repeatable process.

Acknowledgements

The authors acknowledge financial support by the China Scholarship Council (CSC), the Faculty of Engineering and the Environment at University of Southampton, the Royal Society (IE111270) and the Royal Academy of Engineering (1314RECI080). Dr. Shengguo Zhou and Dr. Feifei Zhang provided valuable discussions during sample preparation.

References

1. F. Su and K. Yao: *ACS applied materials & interfaces*, 2014, **6**, 8762-8770.
2. Y. Liu, S. Li, J. Zhang, J. Liu, Z. Han and L. Ren: *Corrosion Science*, 2015, **94**, 190-196.
3. N. Gunari, L. H. Brewer, S. M. Bennett, A. Sokolova, N. D. Kraut, J. A. Finlay, A. E. Meyer, G. C. Walker, D. E. Wendt and M. E. Callow: *Biofouling*, 2011, **27**, 137-149.

4. S. Jung, M. Dorrestijn, D. Raps, A. Das, C. M. Megaridis and D. Poulikakos: *Langmuir*, 2011, **27**, 3059-3066.
5. X. Zhang, Y. Guo, Z. Zhang and P. Zhang: *Applied Surface Science*, 2013, **284**, 319-323.
6. J. Song, S. Huang, Y. Lu, X. Bu, J. E. Mates, A. Ghosh, R. Ganguly, C. J. Carmalt, I. P. Parkin and W. Xu: *ACS applied materials & interfaces*, 2014, **6**, 19858-19865.
7. P. Zhang and F. Lv: *Energy*, 2015, **82**, 1068-1087.
8. I. Malavasi, B. Bourdon, P. Di Marco, J. de Coninck and M. Marengo: *International Communications in Heat and Mass Transfer*, 2015, **63**, 1-7.
9. Z. Chen, F. Li, L. Hao, A. Chen and Y. Kong: *Applied Surface Science*, 2011, **258**, 1395-1398.
10. J. F. Wang, Y. Li, Y. Kong, J. Zhou, J. Z. Wu, X. H. Wu, W. Qin, Z. L. Jiao and L. X. Jiang: *Rsc Advances*, 2015, **5**, 81024-81029.
11. F. Zhang, B. W. Robinson, H. de Villiers-Lovelock, R. J. Wood and S. C. Wang: *Journal of Materials Chemistry A*, 2015, **3**, 13864-13873.
12. C. Liu, F. Su, J. Liang and P. Huang: *Surface and Coatings Technology*, 2014, **258**, 580-586.
13. A. Haghdoost and R. Pitchumani: *Langmuir*, 2013, **30**, 4183-4191.
14. A. El-Sherik and U. Erb: *Journal of Materials Science*, 1995, **30**, 5743-5749.
15. J. Liang, D. Li, D. Wang, K. Liu and L. Chen: *Applied Surface Science*, 2014, **293**, 265-270.
16. W. Li and Z. Kang: *Surface & Coatings Technology*, 2014, **253**, 205-213.
17. S. Huang, Y. Hu and W. Pan: *Surface & Coatings Technology*, 2011, **205**, 3872-3876.
18. S. Esmailzadeh, S. Khorsand, K. Raeissi and F. Ashrafizadeh: *Surface & Coatings Technology*, 2015, **283**, 337-346.
19. F. Tian, A. Hu, L. Ming and D. Mao: *Applied Surface Science*, 2012, **258**, 3643-3646.
20. Z. Chen, L. Hao, A. Chen, Q. Song and C. Chen: *Electrochimica Acta*, 2012, **59**, 168-171.
21. B. Bhushan and M. Nosonovsky: *Philosophical Transactions of the Royal Society of London A: Mathematical, Physical and Engineering Sciences*, 2010, **368**, 4713-4728.
22. S. Shafraniuk: *Cheminform*, 2013, **44**, 9325-9358.
23. E. García-Lecina, I. García-Urrutia, J. Díez, J. Fornell, E. Pellicer and J. Sort: *Electrochimica Acta*, 2013, **114**, 859-867.
24. C. Neinhuis and W. Barthlott: *Annals of botany*, 1997, **79**, 667-677.
25. A. Stalder, G. Kulik, D. Sage, L. Barbieri and P. Hoffmann: *Colloids and surfaces A: physicochemical and engineering aspects*, 2006, **286**, 92-103.
26. A. F. Stalder, T. Melchior, M. Müller, D. Sage, T. Blu and M. Unser: *Colloids and Surfaces A: Physicochemical and Engineering Aspects*, 2010, **364**, 72-81.
27. Y. He, S. C. Wang, F. C. Walsh, W. Li, L. He and P. A. S. Reed: *RSC Advances*, 2015, **5**, 42965-42970.
28. Z. L. Chu and S. Seeger: *RSC Advances*, 2015, **5**, 21999-22004.
29. N. Guglielmi: *Journal of the Electrochemical Society*, 1972, **119**, 1009-1012.
30. M. Miwa, A. Nakajima, A. Fujishima, K. Hashimoto and T.Watanabe: *Langmuir*, 2000, **16**, 5754-5760.
31. C. Gu and T.-Y. Zhang: *Langmuir*, 2008, **24**, 12010-12016.
32. X. Liu: *Soft Matter*, 2012, **8**, 2070-2086.
33. B. Bhushan and E. K. Her: *Langmuir the Acs Journal of Surfaces & Colloids*, 2010, **26**, 8207-8217.
34. A. Cassie and S. Baxter: *Transactions of the Faraday Society*, 1944, **40**, 546-551.
35. Y. R. Uhm, K. Y. Park and J. C. Sun: *Research on Chemical Intermediates*, 2014, 1-9.
36. A. M. Rashidi and A. Amadeh: *Surface & Coatings Technology*, 2009, **204**, 353-358.
37. S. H. Kim, H. J. Sohn, Y. C. Joo, Y. W. Kim, T. H. Yim, H. Y. Lee and T. Kang: *Surface & Coatings Technology*, 2005, **199**, 43-48.
38. M. Stroumbouli, P. Gyftou, E. Pavlatou and N. Spyrellis: *Surface and Coatings Technology*, 2005, **195**, 325-332.
39. S.-C. Wang and W.-C. J. Wei: *Journal of materials research*, 2003, **18**, 1566-1574.
40. Z. She, Q. Li, Z. Wang, L. Li, F. Chen and J. Zhou: *Chemical Engineering Journal*, 2013, **228**, 415-424.
41. Y. H. Wu, W. J. Zhao, W. R. Wang and W. J. Sui: *Rsc Advances*, 2016, **6**, 5100-5110.
42. Z. She, Q. Li, Z. Wang, C. Tan, J. Zhou and L. Li: *Surface and Coatings Technology*, 2014, **251**, 7-14.
43. C. Low, R. Wills and F. Walsh: *Surface and Coatings Technology*, 2006, **201**, 371-383.